PAPER

A multi-scale, multi-physics modeling framework to predict spatial variation of properties in additive-manufactured metals

IOP ebooks™

Bringing you innovative digital publishing with leading voices to create your essential collection of books in STEM research.

Start exploring the collection - download the first chapter of every title for free.

A multi-scale, multi-physics modeling framework to predict spatial variation of properties in additive-manufactured metals

Carl Herriott[1] , **Xuxiao Li[1]**, **Nadia Kouraytem[1]** , **Vahid Tari[2]**, **Wenda Tan[1]**, **Benjamin Anglin[2]** , **Anthony D Rollett[2]** and **Ashley D Spear[1]**

[1] Department of Mechanical Engineering, University of Utah, Salt Lake City, UT, United States of America
[2] Department of Materials Science and Engineering, Carnegie Mellon University, Pittsburgh, PA, United States of America

E-mail: ashley.spear@utah.edu

Abstract

The microstructure of additively manufactured (AM) metals has been shown to be heterogeneous and spatially non-uniform when compared to conventionally manufactured metals. Consequently, the effective mechanical properties of AM-metal parts are expected to vary both within and among builds. Here, we present a framework for simulating process–(micro)structure–property relationships of AM metals produced via direct laser deposition (DLD). The framework predicts grain nucleation and competitive growth as a function of thermal history for a multi-pass, multi-layer DLD process. The resulting three-dimensional microstructure is automatically sub-sampled to perform virtual mechanical testing throughout the build domain using a parallelized elasto-viscoplastic fast Fourier transform code, accounting for grain-boundary strengthening. The effective stress–strain response of each sub-sampled volume is automatically analyzed to extract effective mechanical properties, which are used to generate property maps showing the spatial variability of effective mechanical properties throughout the simulated build volume. As a demonstration, the framework is applied to different DLD stainless steel 316L build volumes having different process-induced microstructures. The multi-physics framework and property maps could provide a path toward qualification of AM-metal parts.

Supplementary material for this article is available online

(Some figures may appear in colour only in the online journal)

1. Introduction

Additive manufacturing (AM), colloquially known as three-dimensional (3D) printing, is a manufacturing technique used for creating 3D structures by adding material in a layer-by-layer fashion. For the last three decades, metal-based AM has gained interest for use in manufacturing of structural parts. Common technologies used in the printing of structural metal AM parts include laser powder bed fusion and direct laser deposition (DLD) [1], in which a high-power-density laser source selectively melts the material for bonding. In contrast to traditional forming or subtractive manufacturing techniques, AM of metals allows relatively fast manufacturing of complex geometries, seamless part consolidation, and relatively little material waste.

Due to rapid solidification during the AM process, the microstructure of laser-processed metals has been shown to be more heterogeneous and exotic compared to conventionally manufactured metals [2]. Efforts have been carried out to create process maps that link the trends of the microstructures to AM process parameters (in terms of the primary process variables) [3–7]. In other studies, efforts are underway to design and locally control the microstructure of AM metals. Dehoff *et al* [8] were able to induce site-specific grain sizes and crystallographic orientation in Inconel 718 by controlling the heat and scan strategy of electron beam AM. These efforts, among others, pave the way towards a better understanding of microstructure variability in metal AM.

Due to the underlying microstructure variation in metal AM, the effective mechanical properties of an AM part are expected to vary within and among builds [9]. That being said, it is crucial to quantify the variability of the effective mechanical properties of AM metal parts to meet the stringent requirements for part qualification in critical structural applications. In this area, Kappes *et al* [10] created a database of experimentally deduced quasi-static mechanical properties of around 3600 Inconel 718 specimens produced via laser powder bed fusion. The results were used to train a machine learning model that could then aid in the design process of AM metal parts by predicting effective mechanical properties of parts printed under certain sets of processing parameters. Such experimentally based studies aid in creating predictive tools for the design of metal AM. However, given the high dimensionality of the AM design space, it is impractical to rely solely on experimentally derived data to establish process–structure–property relationships. Hence, there is a need for simulation efforts to complement experimental testing with virtual testing.

Modeling and simulations provide a path toward creating a feasible qualification framework that closes the gap in the process–structure–property–performance paradigm for AM. A computational framework that is capable of linking the thermal process, resulting microstructures, and mechanical response of metal AM parts would provide a powerful and much-needed tool for engineers to design and qualify AM parts used in critical structural applications. A very recent example of such a framework was presented by Yan *et al* [11]. They presented a predictive simulation framework that combines a thermal-fluid model of molten metals, microstructure generation, and prediction of fatigue life in metal AM. There remains a need to leverage similar process–structure–property tools to predict the variability not only among different builds, but even within the same build.

In this paper, we propose a novel, integrated framework that outputs site-specific property maps within a simulated AM build domain by accounting for relationships among process, microstructure, and properties. This framework is then used to predict the effective mechanical properties of an AM stainless steel (SS) 316L structure produced by DLD. This framework could provide a path towards qualification of AM metal parts by, for example, using it to identify potential hot-spots or unacceptable levels of variability in mechanical properties across the build domain.

For completeness, the next two subsections present the work in the literature that has been carried out on modeling process and mechanical behavior of metal AM. Then, in section 2, the paper includes a description of both the process model and the solid model used in this semi-automated framework. In the first model, we focus on the macroscale thermal modeling and the generation of the synthetic, 3D microstructure for a DLD process. Then, a microstructure-sensitive mechanical model based on a parallelized elasto-viscoplastic fast Fourier transform (EVPFFT) framework is presented, along with the generation of the site-specific property maps. Finally, in section 3, the results of the framework applied to a DLD SS316L structure elucidate the variability of the effective mechanical properties within the AM build.

1.1. Process modeling of additively manufactured metals

On the process modeling of metal-based AM, two primary methods for simulating mesoscale grain structure are available in the literature: the cellular automaton (CA) method [12–16] and the Monte-Carlo (MC) method [17]. In both methods, the grain-structure evolution is determined by the thermal history, i.e. the temperature as a function of time and space. The thermal history is provided either by a simulation or an idealized estimation as an input to the grain-structure simulation.

In their recent articles, Zhang *et al* [12] and Rai *et al* [13] implemented a two-dimensional (2D) CA model. Their results captured the epitaxial nucleation and competitive growth during the grain-structure evolution as well as the consequential grain coarsening caused by the competitive growth. Later, Zinovieva *et al* [15] extended the CA method to be 3D, and investigated the 3D grain structure in a multi-layer, multi-pass build; grain coarsening and a strong texture were reported. However, in these CA models, the nucleation is assumed to occur only at the fusion line, and the potential 'bulk' nucleation ahead of the solidification front is not considered. Improving upon the assumption, Lópeza *et al* [14] took into account the effect of bulk nucleation in their 2D CA model and reported a laminar grain structure. Extending to a 3D CA model, Panwisawas *et al* [16] also considered the bulk nucleation, but only the grain structure from single-pass builds was discussed.

As for the MC model, in a recent study, Rodgers *et al* [17] demonstrated its capability to simulate the grain structure in large builds. However, the crystallographic orientation of grains was not simulated by the MC method. The simulated grain structure in this case matched qualitatively with experimental results. No discussion on the nucleation mechanisms were provided.

In a recent work by the co-authors [18], a 3D CA model was established to investigate the grain structure in a DLD process for SS304. The model included both the epitaxial nucleation at the fusion line and the bulk nucleation ahead of the solidification front. The model was able to duplicate multiple different grain textures that had been found from experiments, and the effects of different nucleation mechanisms on the grain structures were discussed.

1.2. Modeling mechanical behavior of additively manufactured metals

In metal AM, there is an increased interest in simulating the mechanical response. The simulations are generally confined to either macroscale or microscale applications. In the biomedical sector, work has been done by simulating the behavior of metallic AM biomaterials used to mimic bone structure [19, 20]. In one application, Hedayati *et al* [19] investigated the fatigue behavior of an open-cell lattice structure with AM Ti-6Al-4V mechanical properties using a finite-element (FE) model. Similarly, work by Andani *et al* [20] compared experimentally measured and simulated elastic moduli of NiTi open-cell lattice structures with a user material subroutine in Abaqus.

Analytical models are another common method for predicting macroscale mechanical behavior of metal AM. Leuders *et al* [21] used two models for predicting fatigue life based on CT-measured defects (Murakami and Danninger-Weiss), applied them to AM Ti-6Al-4V, and compared the predictions to experimentally measured values. Both models needed adaptations to improve the predictions as they were originally developed for traditionally manufactured metals. Models have also been developed based on processing parameters and experimental results to predict the fatigue life [22] and shear strength, hardness, and density [23] of SS316L manufactured by laser powder bed fusion. Going further, Collins *et al* [24] and Hayes *et al* [25] proposed a method of predicting the yield strength of Ti-6Al-4V using neural networks and genetic algorithms to mine a process–structure–property database to develop a constitutive equation for tensile property prediction.

While the efforts mentioned above do not simulate the microstructure explicitly, there have been other mechanical-modeling efforts reported that consider metal AM microstructures generated through metal AM process modeling. Recently, Ozturk and Rollett [26] formed a synthetic microstructure database of statistically representative dual-phase AM Ti-6Al-4V structures and studied the relative effects of specific microstructural features on the mechanical properties. Ahmadi *et al* [27] simulated an AM microstructure by repeating a melt pool geometry with a grain structure generated via Voronoi tessellation. They simulated the mechanical response using a cohesive zone model and compared the results to experimental observations. Likewise, Andani *et al* [28] used a similar grain-structure model but investigated the response of representative volume elements (RVEs) of interest within the simulated microstructure. While the works by Ahmadi and Andani did consider a simulated microstructure in their mechanical simulations, neither used a physics-based approach to predict the microstructure. Instead, they approximated the microstructure with Voronoi tessellation and recreated the melt pool geometries. However, Yan *et al* [11] developed a physics-based framework linking a powder bed fusion process simulation, grain-growth model, and a self-consistent clustering analysis FE model to predict the fatigue life of Ti-6Al-4V. To explore the variance within their simulated microstructure, they sampled volumes of interest, four in total, from their two-layer build and compared the mechanical response.

It is apparent, from the literature discussed herein, that there is a need to integrate physics-based models to predict microstructure-sensitive mechanical response and its inherent variability through AM-build domains. Doing so will require an efficient approach to enable high-throughput simulation.

2. Methods

A high-level overview of the process–structure–property framework is presented first, and details of each component are provided in following subsections. A graphical representation of the entire process–structure–property framework presented here is shown in figure 1. The
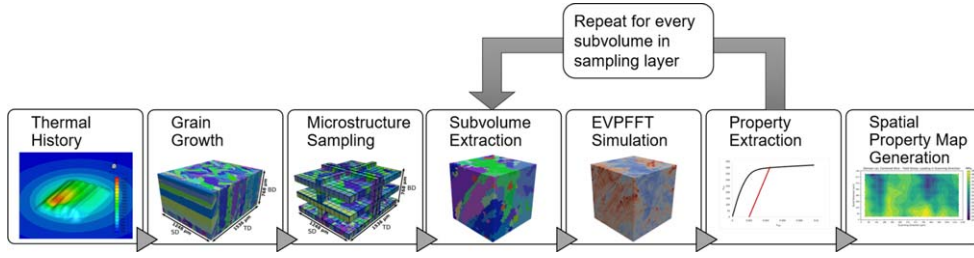
Figure 1. Graphical overview of the process–structure–property framework. Each figure is a representation of the output for each stage of the framework.

framework begins with a thermal history model along with a novel method for grain-structure modeling to simulate a DLD process and the resultant simulated microstructural domain. Next, an area or layer of interest within the microstructure is selected. This layer of interest is divided into individual subvolumes. The full-field response of each subvolume is computed using EVPFFT formulation. From the full-field response, an effective stress–strain curve is extracted and effective mechanical properties are calculated. This process of extracting mechanical properties is repeated on every subvolume within the layer of interest. Once all the properties for each subvolume are known, a site-specific spatial property map is generated. A detailed description of each portion of the framework is presented below.

2.1. DLD process modeling

In this work, a macroscale model based on the finite volume method will be first used to predict the thermal history, which will then be used in a mesoscale CA method to predict the grain growth during molten-pool solidification [29].

2.1.1. Macroscale thermal model. In the macroscale thermal model, as a common assumption for the simulation in metal AM [30], the fluid flow in the molten pool is ignored, and physics are dominated by heat conduction. The governing equation is the heat conduction equation, written in a conservative form as:

$$\frac{\partial(\rho e)}{\partial t} - \nabla \cdot (k \nabla T) = S, \tag{1}$$

where ρ is density, e is internal energy, k is thermal conductivity, T is temperature, and S is the source term. For a DLD process, the source term comes from the laser heating (S_{laser}) and the deposition of powder (S_{add}); we also include in the source term the heat loss from convection (S_{conv}) and radiation (S_{rad}) at the metal–gas interface, as can be expressed by equation (2):

$$S = S_{\text{laser}} + S_{\text{add}} - (S_{\text{conv}} + S_{\text{rad}}). \tag{2}$$

The metal–gas interface in this work is captured by the level-set function and is treated in a diffused manner. That is, all of the material properties such as ρ and k, are treated as the properties of a mixture of metal and gas, and are expressed as functions of the level-set. More details regarding the interface treatment and the calculation of the source terms in equation (2) are found in [31, 32].

The computation domain used in the thermal simulation is shown in figure 2(a). The three axes are the scanning direction (SD), build direction (BD), and transverse direction (TD). The laser scans in the TD-SD plane and the part is built layer-by-layer in the +BD
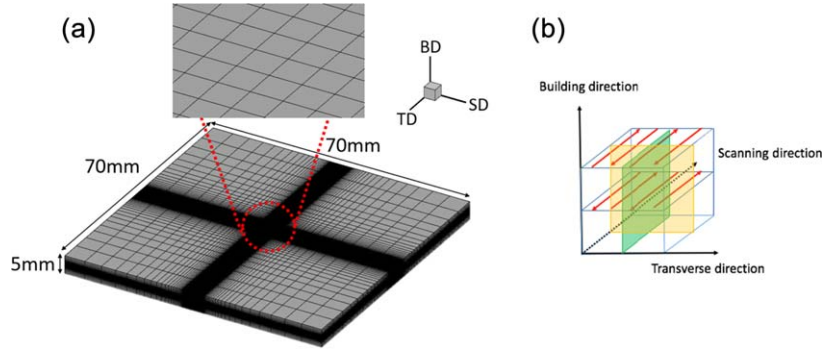
Figure 2. (a) The computation domain and the mesh for the FV simulation to predict the thermal history [18]. (b) The laser scanning strategy used to simulate a direct laser deposition process. The red arrows represent the alternating scanning path of the laser. Reprinted from [18], Copyright 2018, with permission from Elsevier.

direction. A non-uniform Cartesian mesh is used, as shown in figure 2(a). The laser only scans in the fine mesh region (circled by the red dashed line) to guarantee an accurate thermal gradient around the molten pool. The coarse mesh around the fine mesh is used to provide a heat sink to avoid non-physical heat accumulation. An insulating boundary condition is applied to all the boundaries of the computation domain. The laser scanning pattern is shown in figure 2(b). In each layer, the laser scans in an alternating pattern along the SD and the laser changes the starting SD by 180° every layer, as indicated by the red arrows in figure 2(b). The output of this step of the framework is the thermal history as a function of space and time for the simulated DLD process.

2.1.2. Mesoscale grain-growth modeling. The thermal history obtained from the macroscale thermal simulation is interpolated in both space and time for the mesoscale CA simulation. The interpolated thermal history then governs the microstructural evolution. The substrate and the shape and crystal orientation for each nucleated grain result from the algorithms in [18] and from the competitive grain growth determined by the 3D CA method in [32]. The nucleation and 3D CA methods are described next.

Epitaxial nucleation: it is assumed that the epitaxial nucleation occurs as soon as the temperature of a cell on the fusion line drops below the liquidus temperature, T_L. A nucleus is added to this cell and it will inherit the same crystallographic orientation as a neighboring solid cell in the underlying layer.

Bulk nucleation: it is assumed that the nucleus density, N, is a continuous function of the undercooling, $\Delta T = T_L - T$ [33]:

$$N = \int_0^{\Delta T} \frac{dN}{d(\Delta T')} d(\Delta T'), \tag{3}$$

where $dN/d(\Delta T)$ is a function of ΔT describing the increase of nuclei density with the increase of undercooling. We assume $dN/d(\Delta T)$ as a Gaussian distribution:

$$\frac{dN}{d(\Delta T)} = \frac{N_0}{\Delta T_\sigma \sqrt{2\pi}} \exp\left(-\frac{\Delta T - \Delta T_c}{\sqrt{2}\,\Delta T_\sigma}\right), \tag{4}$$

where N_0, ΔT_c, and ΔT_σ are three nucleation parameters characterizing the bulk nucleation condition. Their physical meaning is shown in figure 3. When the undercooling is around the
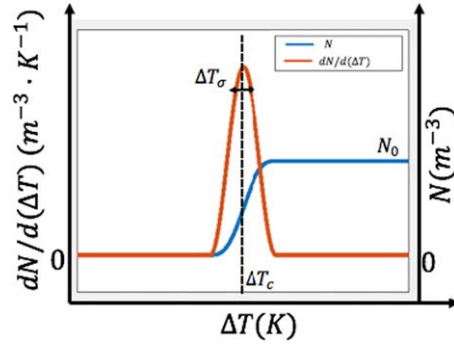
Figure 3. Nucleation parameters of the continuous nucleation model. Reprinted from [18], Copyright 2018, with permission from Elsevier.

interval ($\Delta T_c - \Delta T_\sigma$, $\Delta T_c + \Delta T_\sigma$), the nuclei density jumps from zero to the maximum nuclei density, N_0, with a random crystal orientation assigned to each nucleus. The three nucleation parameters N_0, ΔT_c and ΔT_σ have to be determined by experiment [33, 34]. In the absence of direct experimental observations, a parametric study was conducted to investigate the effect of the parameters on the resulting grain structure [18].

Grain growth: the grain growth after nucleation is simulated by the CA method. Essentially, the CA method assumes the grain growth velocity is a function of the local undercooling, and explicitly tracks the outer contour of each grain by the de-centered octahedron scheme [29]. In this work, we use a polynomial to fit the dendrite growth simulation result from [32] to approximate the growth velocity, V_{growth}, of grains for a given metal, as shown by equation (5):

$$V_{growth}(\Delta T) = a(\Delta T)^3 + b(\Delta T)^2 + c\Delta T + d, \tag{5}$$

where a, b, c, d are fit to the given metal, ΔT is in Kelvin, and V_{growth} is in m s^{-1}. In this competitive grain-growth model, grains growth preferentially along specific crystallographic directions ($\langle 001 \rangle$ for fcc and bcc materials). This competitive growth leads to the formation of crystallographic texture that has been shown to be similar to that from experiment [18]. For further details regarding of the implementation of the CA method, the reader is referred to [32]. The output from the grain-growth model is a 3D, voxel-based domain, where each voxel has a grain ID and crystal orientation assigned to it.

2.2. Microstructure-sensitive mechanical modeling

2.2.1. Automated subvolume sampling. The simulated AM build domain serves as the input to the microstructure-sensitive mechanical modeling section of the framework. The 3D build domain is automatically divided into discrete subvolumes that will undergo virtual mechanical testing.

It is important to have a sufficient number of subvolumes within a domain to capture the desired resolution in the spatial property maps, while at the same time defining the subvolumes to exploit computational efficiency.

Although it is possible to discretize the entire build domain, it is not required and, in fact, might be of interest to a user to investigate a specific layer or layers within the build domain, as demonstrated in the example application described in section 3.2. Each microstructural subvolume is passed into DREAM.3D, an open-source software for digitally representing 3D

microstructures [35]. DREAM.3D is used to record a number of microstructural statistics (e.g. average grain volume and aspect ratio) [36] and to write the input file for the EVPFFT model. The HDF5 scheme, which provides a portable, binary format, is used to store the image along with orientation data.

2.2.2. Parallelized EVPFFT framework. It is well known that the deformation of polycrystalline materials is heterogeneous at the grain scale when the polycrystal is subjected to an external loading. The heterogeneity at grain scale is due to differences in orientation among neighboring grains combined with the anisotropic elastic and plastic response of single crystals. Full-field crystal plasticity codes such as crystal plasticity finite element method (CPFEM) or crystal plasticity fast Fourier transform (CPFFT) are well established methods to predict the local heterogeneity of a polycrystalline volume. In CPFEM calculations [37–39], a solution is given for the equilibrium of forces and the compatibility of displacements using the principle of virtual work for a microstructural volume discretized using a finite-element mesh. CPFFT is an alternative full-field crystal plasticity implementation introduced by Lebensohn [40] following the pioneering work of Suquet and co-workers [41, 42]. In CPFFT formulations, the governing equations for heterogeneous media with periodic boundary conditions are solved by applying an FFT-based algorithm in conjunction with Green's function method (e.g. see Mura [43]). CPFFT is computationally more efficient compared to CPFEM for same-size problems since FFT does not require the inversion of a large stiffness matrix for the global solution [44].

　Furthermore, unlike CPFEM, the CPFFT method does not suffer from the challenges associated with creating meshed microstructures, which is non-trivial. For example, an entire thesis has been devoted to microstructure representation using meshes [45].

　In this framework, we use the EVPFFT formulation by Lebensohn *et al* [46], which is an adaptation of CPFFT to the EVP regime for capturing full-field elastic and plastic grain interactions of 3D polycrystalline aggregates. This is implemented within the parallelized code, Micromechanical Analysis of Stress–Strain Inhomogeneities with fast Fourier transforms (MASSIF), to compute the full-field micromechanical response of each subvolume. MASSIF/EVPFFT is based on small strain formulation and uses the following constitutive relation between local stress and strain:

$$\varepsilon_{ij}(x) = \varepsilon_{ij}^e(x) + \varepsilon_{ij}^p(x) = C_{ijkl}^{-1}(x)\sigma_{kl}(x) + \varepsilon_{ij}^{p,t}(x) + \dot{\varepsilon}_{ij}^p(x,\sigma)\Delta t, \tag{6}$$

where $\varepsilon_{ij}(x)$ is the local strain as a summation of local elastic strain $\varepsilon_{ij}^e(x)$ and local plastic strain $\varepsilon_{ij}^p(x)$. Local elastic strain is calculated via Hooke's law $C_{ijkl}^{-1}(x)\sigma_{kl}(x)$, where $\sigma_{kl}(x)$ and $C_{ijkl}^{-1}(x)$ are local stress and local stiffness at each grid point. Plastic strain after each time increment, Δt, is calculated based on an Euler discretization for the time integration of the local plastic strain rate, which is given by:

$$\dot{\varepsilon}_{ij}^p(x) = \dot{\gamma}_0 \sum_{s=1}^{N_s} m_{ij}^s(x) \left(\frac{|m_{kl}^s(x)\sigma'_{kl}(x)|}{\tau^s(x)} \right)^n \times \mathrm{sgn}(m_{kl}^s(x)\sigma'_{kl}(x)), \tag{7}$$

where $\dot{\gamma}_0$ is a reference shear rate, N_s is the total number of slip systems, m^s is the symmetric Schmid tensor for each slip system, σ' is the deviatoric stress tensor, τ^s is the critical resolved shear stress (CRSS) in slip system s, and n is the rate-sensitivity exponent. The local CRSS and Schmid tensor are updated at the end of each strain step. The evolution of local CRSS at each point is calculated in this work by the Voce hardening law given by:

$$\Delta\tau^\alpha = \frac{\mathrm{d}\bar{\tau}^\alpha}{\mathrm{d}\Gamma} \sum_\beta h^{\alpha\beta}\dot{\gamma}^\beta, \tag{8}$$

$$\bar{\tau}^\alpha = \tau_0 + (\tau_1 + \theta_1\Gamma)\left[1 - \exp\left(-\frac{\theta_0\Gamma}{\tau_1}\right)\right], \tag{9}$$

where $\bar{\tau}^\alpha$ is the CRSS in slip system α, $h^{\alpha\beta}$ is the latent hardening relating slip activity in slip system β with the hardening of slip system α, $\dot{\gamma}^\beta$ is the shear rate of slip on system β, Γ is the accumulated slip across all slip systems, and τ_0, τ_1, θ_0, θ_1 are the Voce hardening law parameters.

A new modification has been incorporated into the MASSIF/EVPFFT program to account for the effects of grain-boundary strengthening, which is reported for the first time here. Contrary to the strain-gradient theory for grain-boundary strengthening, here we take a stress-based approach inspired by the work of Chakravarthy and Curtin [47]. Crystallographic orientation and the possible slip directions are used to find the directed Euclidean distance to the nearest grain boundary at each point in the input microstructure prior to the MASSIF/EVPFFT calculation. The *directed distance* is defined as the distance parallel to the Burgers vector and therefore in the slip plane of each slip system. This directed distance, d_{GB}, is then used to scale the initial CRSS, τ_0, according to the following empirical relationship at the slip-system level, akin to the macroscale Hall–Petch effect:

$$\tau_0 = \tau_\infty + \frac{k_{\mathrm{GB}}}{d_{\mathrm{GB}}\,v_{\mathrm{size}}}, \tag{10}$$

where d_{GB} is the directed distance from a given voxel to the nearest grain boundary and is measured in units of voxels. This distance is scaled by v_{size}, the specified voxel size (e.g. in units of μm/voxel). The parameter τ_∞ corresponds to τ_0 for a specimen with an infinitely large grain size, and k_{GB} is the rate at which τ_0 changes with distance to the nearest grain boundary.

In the current implementation of the framework, each subvolume is subjected to uniaxially applied displacement using the MASSIF/EVPFFT code. The simulations can be repeated for different directions of applied displacement, if, for example, calculation of anisotropy is desired. To run a simulation, MASSIF requires the crystal orientation of each grain, a strain rate, the number of steps, and the cubic elastic constants and Voce hardening parameters. The parallel HDF library [48] was implemented in the parallel MASSIF code using an MPI package. The parallel implementation enables simulations of subvolumes within the build domain to be computed relatively rapidly when compared to, say, CPFEM. The computational efficiency allows for the generation of spatial property maps, described next. More information regarding the efficiency and validation of the parallelized MASSIF implementation can be found in [49].

2.3. Generation of site-specific property maps

2.3.1. Automated calculation of effective mechanical properties. The full-field responses predicted by the MASSIF simulations are used to calculate effective (homogenized) mechanical properties for each subvolume. First, an effective stress–strain curve is generated by averaging all the deviatoric stress and strain components for each voxel across the entire subvolume. The von Mises equivalent stress and strain are then calculated using the averaged components. This process is repeated for each displacement step until the effective stress–strain curve is generated.

Table 1. Process parameters of direct laser deposition (DLD).

Laser power (W)	200
Scanning velocity (mm s^{-1})	26
$1/e^2$ Beam diameter (μm)	440
Hatch spacing (μm)	250

Table 2. Thermal properties of SS316L [31].

Property	Stainless steel 316L	
	Solid	Liquid
Density (kg m^{-3})	8000	8000
Specific heat (J kg^{-1} K^{-1})	500	500
Thermal conductivity (W m^{-1} K^{-1})	19.2	209
Liquidus temperature (K)		1673
Solidus temperature (K)		1648
Melting latent heat (J kg^{-1})		250 000

From the effective stress–strain curve, effective mechanical properties are calculated, namely the effective Young's modulus, E_{eff}, and the effective yield strength, $\sigma_{y,\text{eff}}$, both in the direction of applied displacement. The Young's modulus is found by applying a Hough transform to the stress–strain response. The Hough transform is a technique that finds the probability that a shape or feature is present in the given data [50]. The feature in this case is a line, $y = mx + b$, that corresponds to the elastic region of the data where the slope of that line is the Young's modulus. With the Young's modulus, a 0.2% yield offset is applied to the curve to approximate the yield strength. This automated process is repeated for every simulated subvolume.

2.3.2. Graphical representation of property maps. Once the effective mechanical properties are calculated for every subvolume, the framework generates spatial-property maps for each loading direction in the form of a filled contour plot. On the map, each grid cell is representative of a subvolume, and the effective mechanical properties are assigned to the centroid of the respective subvolume. The gradient between neighboring subvolumes is dependent on the contour plotting algorithm. For reference, vertical lines are plotted to represent the laser scan tracks, and all coordinates are local to the dimensions of the layer under investigation.

3. Framework application to SS316L: results and discussion

As a demonstration, the framework described above is now applied to multiple instances of SS316L produced via DLD.

3.1. DLD process model

The process parameters and thermal properties used in the simulation of SS316L are listed in tables 1 and 2, respectively. The constants used in equation (5) are: $a = 1.0909 \times 10^{-5}$,
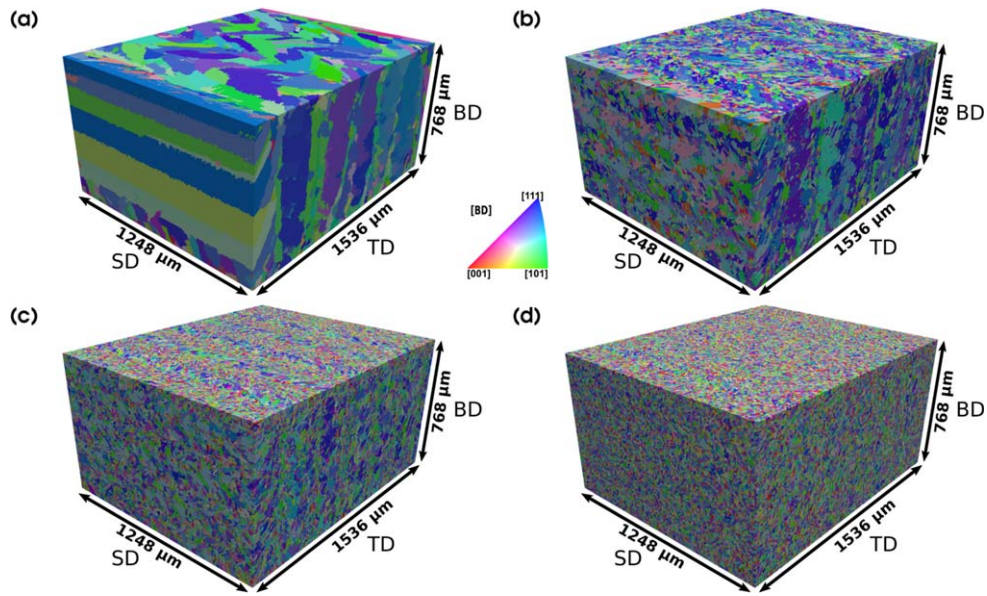
Figure 4. A 3D representation of each simulated microstructure generated by varying the nucleation parameters. (a)–(d) Domains A–D, respectively.

Table 3. Grain-nucleation parameters for each microstructural domain.

Domain	N_0 (m^{-3})	ΔT_c(K)
A	10^{13}	10
B	10^{14}	0
C	10^{15}	5
D	10^{15}	0

$b = -2.0336 \times 10^{-4}$, $c = 2.7397 \times 10^{-3}$, $d = 1.1505 \times 10^{-4}$. The simulation domain is discretized using an element size of 25 μm for the thermal model and a cell size of 3 μm for the 3D CA model. An average grain size of 25 μm is assumed for the substrate.

An eight-layer build domain is simulated, with six passes in each layer and $\sim$250 μm between the centerlines of the scan tracks. For the three nucleation parameters, N_0, ΔT_c, and ΔT_σ, we fix ΔT_σ to be a negligible number, as the effects of ΔT_σ on the grain structure are found to be insignificant. Then, four combinations (labeled domains A–D) of (N_0, ΔT_c) are used to explore possible grain structures, as listed in table 3.

The grain-nucleation parameters are chosen such that nucleation occurs increasingly frequently from domain A to D. 3D views of domains A–D are shown in figure 4. The extents of the TD, SD, and BD dimensions are 1536, 1248, and 768 μm, respectively. A 2D view of the resulting microstructures in the SD-BD plane is shown in figure 5. The selected nucleation parameters result in relatively large, elongated, and tortuous grains in domain A. The grains become smaller and more equiaxed moving from domains A to D.
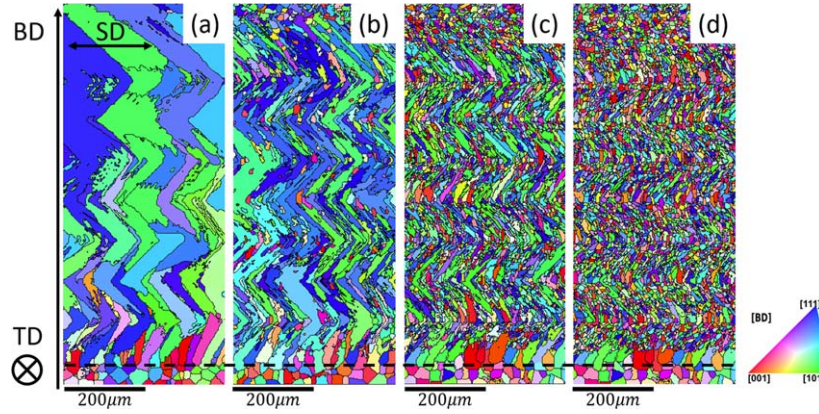
Figure 5. Cross-sectional views of the SD-BD plane for each microstructural domain obtained by varying N_0 and ΔT_c. (a) Domain A: $N_0 = 10^{13}$ m^{-3}, $\Delta T_N = 10$ K; (b) domain B: $N_0 = 10^{14}$ m^{-3}, $\Delta T_N = 0$ K; (c) domain C: $N_0 = 10^{15}$ m^{-3}, $\Delta T_N = 5$ K; (d) domain D: $N_0 = 10^{15}$ m^{-3}, $\Delta T_N = 0$ K. The black dashed line indicates the location of the fusion line from the first layer.

Table 4. Cubic elastic constants [51], Voce hardening parameters [52], and distance hardening parameters for SS316L.

Cubic elastic constants (MPa)	C_{11}	C_{12}	C_{44}
	204 600	137 700	126 200
Voce hardening parameters (MPa)	τ_1	θ_0	θ_1
	70	105 000	410
Distance hardening parameters	τ_∞ (MPa)	k_{GB} (MPa μm^{-1})	v_{size} (μm/ voxel)
	10	300	3

3.2. Microstructure-sensitive mechanical modeling

The single-crystal elastic constants are needed by MASSIF to compute the elastic response of each microstructual subvolume. In this example, with SS316L and SS304 being from the same austenitic family, the values of the cubic elastic constants for the current example of SS316L are approximated from those of SS304 [51], which are provided in table 4. In each iteration of MASSIF, the CRSS values are obtained from the extended Voce hardening law, seen in equation (9). The values of the Voce hardening parameters, shown in table 4, are taken from [52] and correspond to a warm-rolled SS316L sheet sample. The three parameters used in the distance hardening function to modify the initial CRSS are given in table 4 as well. The values of the parameters were selected to exploit the grain-size sensitivity of the model while still producing a realistic range of values for CRSS.

The specified voxel size is 3 μm, and the chosen subvolume size is $32 \times 32 \times 32$ voxels or $96 \times 96 \times 96$ μm. To verify the stress response at this voxel size, a convergence study was performed by doubling the voxel resolution of a subvolume, applying a displacement using MASSIF, and comparing the effective stress–strain curve to that using the original
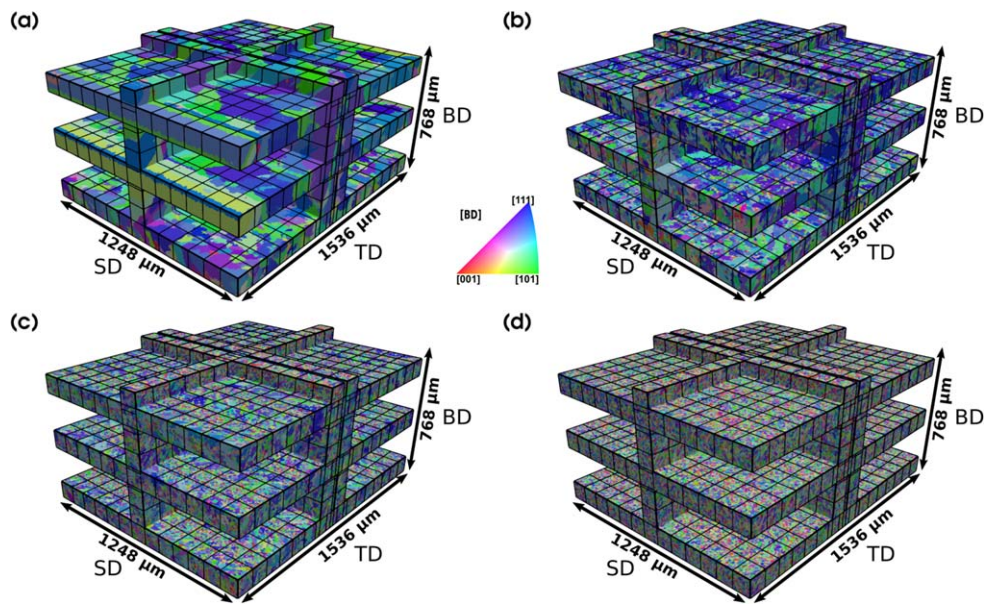
Figure 6. A 3D representation of the sampling layers and subvolumes defined for each domain. (a)–(d) Domains A–D, respectively.

resolution. There was found to be less than one percent difference between the resulting curves, so the original resolution, 3 μm, is kept. The subvolume size is selected to be approximately the same height as a single build layer, which is ∼100 μm. The subvolume sampling strategy used in this example is shown in figure 6. The sampling locations within the TD-SD plane are taken at the first, fourth, and seventh build layers, corresponding to BD coordinates of 0–96, 300–396, and 600–696 μm, respectively, with each layer comprising 208 subvolumes. These sampling layers where chosen to investigate the variability within an AM domain as it is built. The two sampling locations within the SD-BD plane are centered along the third track, at TD coordinates 752–848 μm, as well as between the third and fourth tracks, at TD coordinates 927–1023 μm. The SD-BD sampling layers each contain 104 subvolumes. These locations were picked to explore any discrepancies that might appear between and along scan lines. The sampling location within the TD-BD plane contains 128 subvolumes and is centered in the SD, at SD coordinates 576–672 μm. In total, 960 subvolumes are simulated for each DLD domain using MASSIF. Furthermore, two simulations are run for each subvolume; one simulation of uniaxially applied displacement equivalent to 1% engineering strain is applied for each in-plane direction of the given sampling-layer plane. Among all four build domains considered in this work, a total of 7680 microstructure-sensitive numerical simulations were completed.

A single subvolume required approximately three to four minutes on eight processors to run the microstructure-sensitive mechanical modeling portion of the framework.

A subset of results for the full-field MASSIF simulations is shown in figure 7. In the figure, two microstructural subvolumes are called out for each of the four build domains. The corresponding von Mises stress field is depicted at 1% engineering strain applied in the TD. Of note for the examples shown in figure 7 is the variability in the stress fields among the build domains but also within the same domain. This variability is visually apparent in Domains A and B and perhaps less so in domains C and D. The variability in the full-field
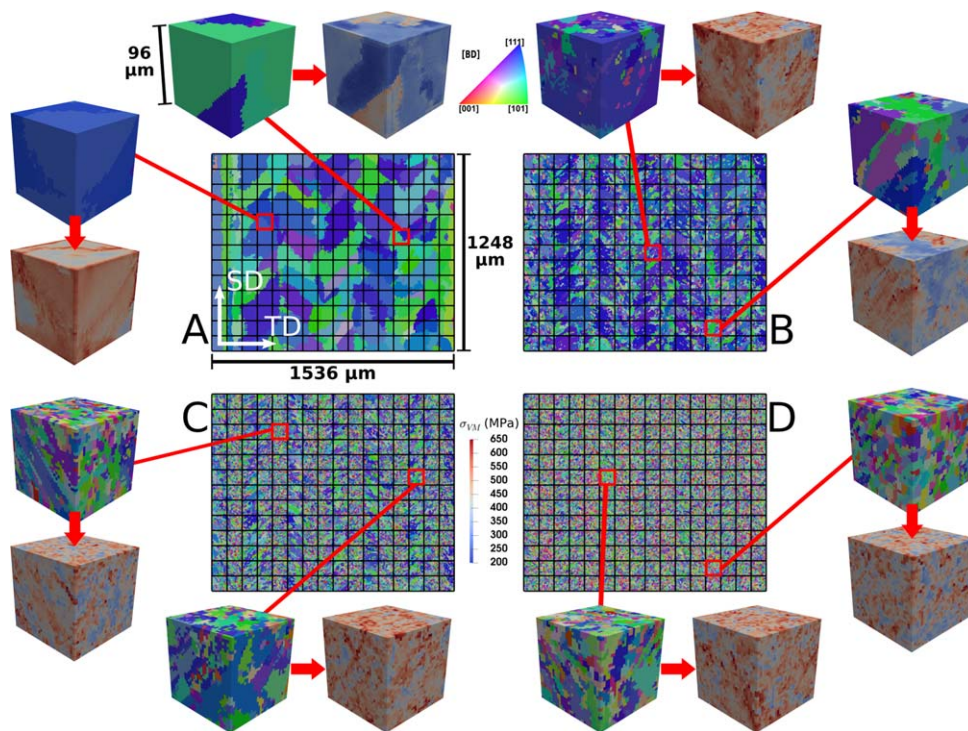
Figure 7. Selected full-field MASSIF/EVPFFT results from the seventh sampling layer in the TD-SD plane for each domain highlighting the variability in responses throughout the layer. For each build domain, two microstructural regions are called out, along with their respective full-field responses due to loading in the SD direction at 1% nominal strain. The colors for the microstructures and full-field responses correspond to the legends for the inverse pole figure and von Mises stress, respectively.

responses due to microstructure sensitivity ultimately translates to variability in the spatial property maps, which is discussed next.

3.3. Site-specific spatial property maps

Once each full-field calculation is complete, the framework automatically extracts the equivalent stress–strain response and calls the Hough-transform function to extract E_{eff} and $\sigma_{y,\text{eff}}$, as described in section 2.3. Figure 8(a) shows the effective mechanical response of every simulated subvolume in the TD-SD plane, with loading applied in the TD direction. Experimental results from [52] are shown as a comparison. Recall that the material used in [52] was a conventionally manufactured, warm-rolled SS316L sheet material. Applying the Hough-transform function to this experimental curve resulted in a calculated yield stress of 268 MPa, which falls in the lower range of $\sigma_{y,\text{eff}}$ from domain A. In the literature, DLD SS316L has been shown to have a much higher yield strength than its traditionally manufactured counterpart, typically in the range of 400–550 MPa [53–55].

An example of the effective yield strength with respect to the average grain size of each subvolume is shown in figure 8(b). Loading is applied in the TD direction. The average grain size is the averaged equivalent spherical diameter of each grain in a specific subvolume [36]. As shown in both plots of figure 8, the distributions of the effective mechanical response and
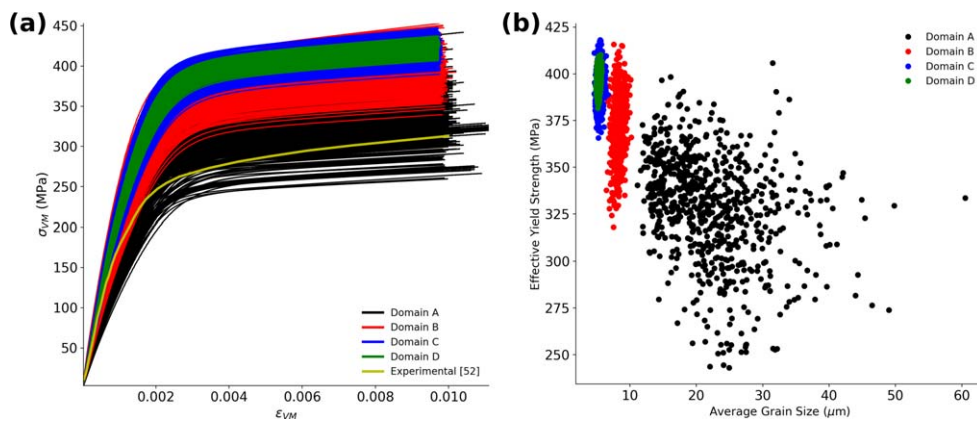
Figure 8. (a) Effective stress–strain curve variance for all 3008 subvolumes in the TD-SD plane for all build domains. Loading is in the transverse direction (TD). Experimental curve of warm-rolled, traditionally manufactured SS316L sheet material from [52] is shown for comparison. (b) Effective yield strength from loading in the TD direction for all domains compared to the average grain size. Each point represents the response of a specific subvolume. Grain size is based on the diameter of a sphere having the equivalent volume of a given grain [36].

the effective yield strength become tighter moving from domain A to D. This is most likely related to the relative size of the grain structure. That is, since the size of the subvolumes are fixed yet grain size varies among the builds, domain D generally has more grains per sub-volume than domain A. As a result, the effective response of a given subvolume in domain A is much more sensitive to the configuration and crystal orientations of the grains within that subvolume as compared to domains B–D. On the other hand, domain D contains a sufficient number of grains per subvolume that the responses better represent the effective response of the material. This observation touches on an important point regarding RVEs, or RVEs. Recall that the goal of this work is to highlight the variability in mechanical response on the scale of something physically meaningful (in this case, the build-layer thickness). This goal is philosophically different than that of defining RVEs. In fact, the establishment of an RVE size for AM metals could become ambiguous and difficult to define, as even the 'representative' response might vary throughout the built part due to both long-range microstructural varia-bility and also to geometrical and surface effects. While the particular issue of RVE definition is beyond the scope of this study, it would certainly be of interest for future studies, which could be enabled by the framework presented here.

Another noteworthy observation from figure 8(b) is that the modification of the CRSS based on the distance-to-nearest-grain-boundary calculation described in section 2.2.2 appears to capture the expected Hall–Petch effect. Specifically, the yield strength values appear generally to increase from domain A (higher average grain size) to domain D (lower average grain size), with a few exceptions that are most likely related to crystal orientation relative to load direction. This trend was not observed prior to making the modification for grain-boundary strengthening. This can also explain why the majority of the responses have higher yield strength values than the experimental results from [52] (yellow curve in figure 8(a), from which the Voce hardening parameters were taken). Recall that the modification to the constitutive model input, described in section 2.2.2, effectively increases the nominal CRSS

based on proximity to a grain boundary, to emulate the effects of grain-boundary strengthening.

The effective mechanical properties, E_{eff} and $\sigma_{y,\text{eff}}$ for each in-plane loading direction, are then used to generate spatial property maps for the SS316L domains according to the procedure described in section 2.3.2. This step resulted in 24 spatial property maps per domain. Since this results in too many figures to reasonably show and discuss, a qualitative discussion of select results will be presented, with focus placed on the effective yield strength. It is noted that the property maps for E_{eff} and $\sigma_{y,\text{eff}}$ show similar trends. All data for generating property maps, including those maps not shown, can be found in the supplementary material available online at stacks.iop.org/MSMS/27/025009/mmedia.

Figure 9 contains spatial-property maps from the TD-SD plane of each domain. The maps show the effective yield strength for each in-plane loading direction and the sampling location is the seventh build layer. In figure 9, the variance in the effective yield strength decreases from domain A (top set) to domain D (bottom set). This follows the trend in figure 8 based on the decreasing grain size, as described above. There is also a notable difference in the response based on the direction of the applied displacement. Loading in the SD direction appears to be stronger than the TD direction. This is substantiated by figure 10, which is a distribution of the ratio $\sigma_{y,\text{eff}}^{\text{TD}}/\sigma_{y,\text{eff}}^{\text{SD}}$ for every build domain. As shown in figure 10, the majority of subvolumes from each domain have a $\sigma_{y,\text{eff}}^{\text{TD}}/\sigma_{y,\text{eff}}^{\text{SD}}$ ratio lower than unity. Figure 10 also shows the same distribution tightening from domain A to D, with the peak of the ratio moving closer to a ratio of unity, which implies that smaller grains and more frequent bulk nucleation tend to remove some of the anisotropy of the simulated microstructural domain.

The above observations regarding anisotropy can be compared to experimental observations from the literature for both conventionally manufactured and AM metals. Experimentally, Moverare and Odén [56] investigated the elastic and plastic anisotropy of a hot and cold rolled duplex SS, designated SAF2304. The material had grain sizes of 0.5–3 μm, which are most comparable to the grain sizes from domain D, yet still significantly smaller. For the austenitic phase, which is more analogous to the material presented here than the ferritic phase, Moverare and Odén found that the *r*-value, or the plastic-strain ratio, is close to a value of unity, with slightly more plastic deformation occurring in the TD than the rolling direction. The crystallographic texture of the austenitic phase and its intensity, measured through x-ray diffractometry, where found to have no significant variation when measured at various depths below the top surface of the material. Correspondingly, there was insignificant variation of plastic anisotropy through the depth of the material. Looking at AM materials, Debroy *et al* [1], compiled and tabulated the macroscopic longitudinal (scanning direction) yield strengths and transverse yield strengths for various AM alloys manufactured with both DLD and powder-bed processes, as reported in literature. While scanning strategies and processing parameters differ among the materials listed, comparisons of the values can be made to get a general sense of the anisotropy in the yield strength for various AM alloys. For austenitic SSs manufactured by DLD and powder-bed processes, the longitudinal yield strength was typically higher, although the difference was less pronounced for powder-bed parts. For the titanium and aluminum alloys, little anisotropy was observed based on the transverse and longitudinal yield strengths. The results discussed here provide some basis for comparison with the simulated anisotropy values presented in figure 10.

In the TD direction of loading, domains A and B have fairly random distributions of properties, but moving to C and D, a pattern emerges in the form of a periodicity with the laser scan tracks (black vertical lines). This periodicity shows that the effective yield strength
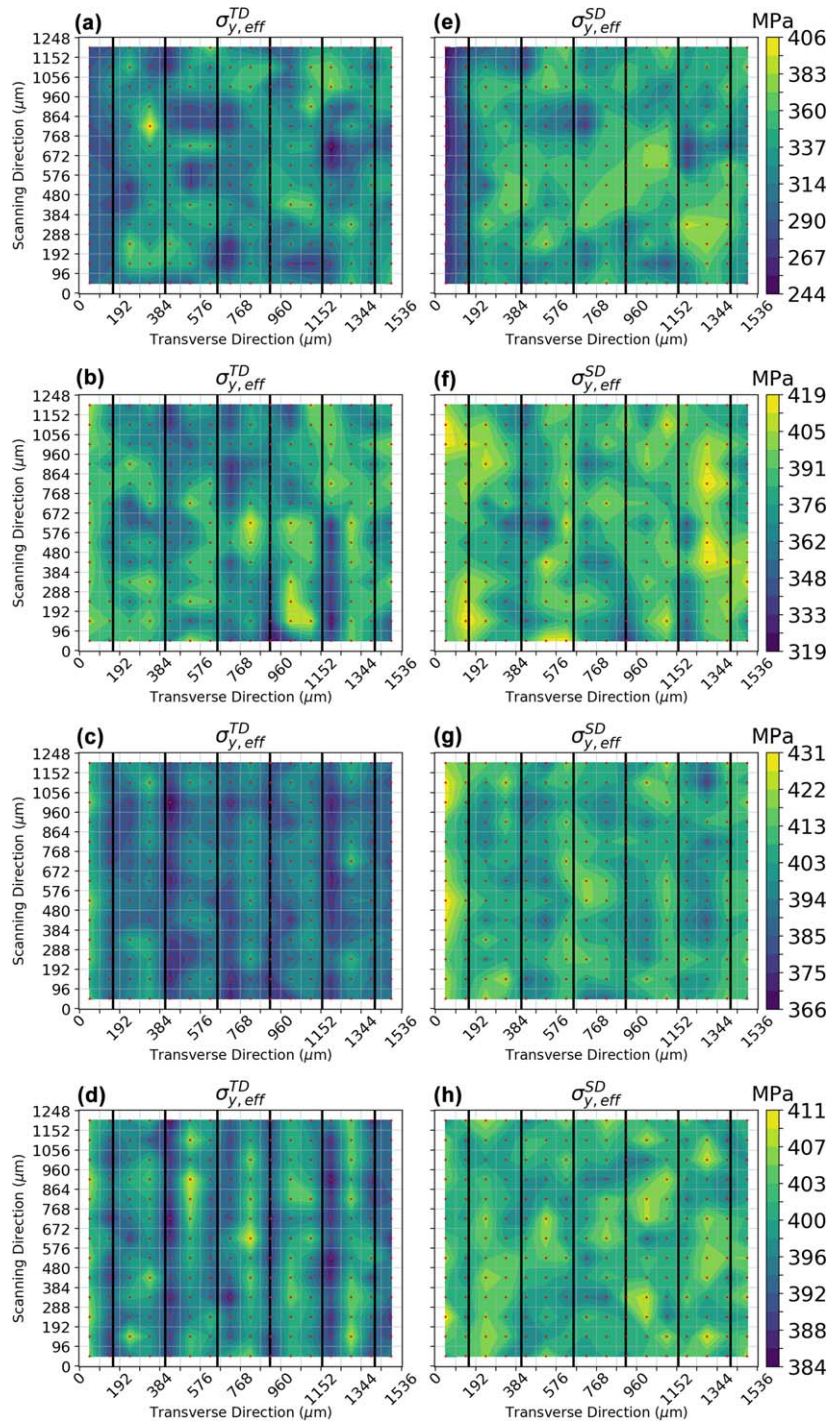
Figure 9. Spatial property maps of $\sigma_{y,\text{eff}}^{\text{TD}}$ (a)–(d), and $\sigma_{y,\text{eff}}^{\text{SD}}$ (e)–(h), for the seventh build layer of each domain. Each set of figures corresponds to a build domain: A (a), (e); B (b), (f); C (c), (g); D (d), (h).

17
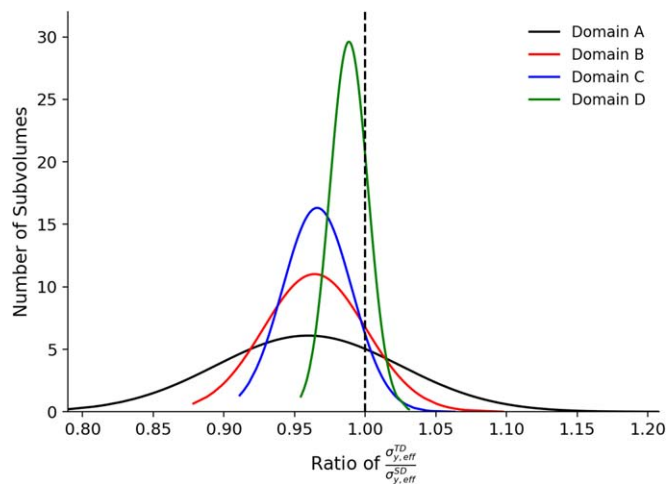
Figure 10. Distribution of effective-yield-strength ratios depicting the differences in plastic anisotropy among four different AM build domains for SS316L.

between scan lines tends to be higher than that directly along the scan line. The $\sigma_{y,\text{eff}}^{\text{TD}}$ periodicity trend apparent in domain D is visible not only throughout the build domain, but in other sampling layers as well. Figure 11 compares the maps from TD-SD plane (figures 11(a)–(c)) to the TD-BD plane map (figure 11(d)) from domain D. Effective yield strength values are from the applied displacement in the TD direction, as that is the common axis between the two planes. Looking at figure 11(d), the same periodicity is apparent, alternating between the scan lines. As shown in figures 11(a)–(c), the properties and trends seen are fairly consistent throughout the build, likely due to the consistent grain size from layer to layer. Interestingly, a similar periodicity has been observed in experimental work by Hayes *et al* [25]. In that work, the authors observed strongly textured vertical bands that formed in an AM Ti-6Al-4V volume produced via wire-fed directed energy deposition. Tensile samples were extracted along and between the textured bands (labeled zone A and B in [25]), and the authors found that these adjacent bands exhibited different values and variances of mechanical properties. Although qualitative comparisons can be drawn between the simulation results presented in this work and the experimental results presented in [25], it is not possible to make a more direct comparison given the significant differences between the AM methods and materials. Similar measurements could be made for DLD SS316L to enable a rigorous and quantitative comparison for experimental validation.

While not explicitly shown, loading in the BD direction tends to produce the same patterns as loading in the TD direction, e.g. the periodicity in figure 11(d) is visible when loading in the BD direction. However, this same periodicity is lost when loading in the SD direction, which is visible in figures 9(d), (h). In fact the property distribution when loading in the SD direction remains fairly random within all four simulated build domains.

4. General remarks and discussion

The study of the spatial variability of mechanical properties in AM metals is an important topic for the qualification of AM-produced parts to be used in structural applications. Physical experiments are generally destructive, costly, and limited in the amount of information that
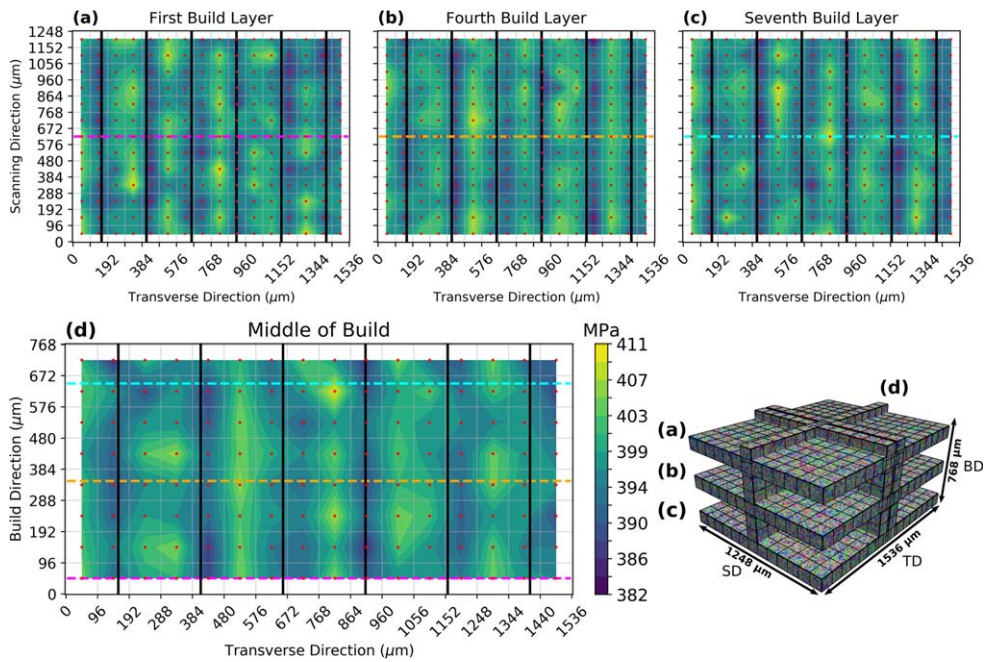
Figure 11. Comparison of effective yield stress property maps of domain D from the TD-SD plane (a)–(c) to the map from the TD-BD sampling plane (d). The loading direction is the common axis shared between the two sampling planes, the transverse direction. The 3D representation of the sampling layers (bottom right) and the dashed colored lines highlight where each sampling layer and corresponding property map intersect within the build domain.

they can provide. Hence, a combination of modeling process-sensitive microstructures followed by simulation of loading on individual microstructural domains provides a powerful tool to fill the gap in understanding of the process–(micro)structure–property of metal AM. In this paper, we proposed a semi-automated multi-scale, multi-physics framework that simulates thermal history and microstructural evolution during DLD and outputs spatially dependent property maps at different locations of interest within the structure. This framework provides a significant advancement in the understanding of the process–(micro)structure–property relationship and presents a relatively efficient technique to highlight the existence of potential hot spots (e.g. regions of low yield strength) within the AM part prior to (or alongside) physically building the part. The framework has potential to be extended to other metals and AM processing parameters.

Despite the capabilities demonstrated above, there are a number of opportunities to improve the framework. Firstly, the simulated microstructures should be validated using microstructural data of similarly processed AM metal parts. At this stage, multiple material parameters are used in the generation of the synthetic microstructure, but it will be important to be able to relate the material parameters to the processing parameters by validating the simulated microstructural domains to those measured experimentally. Experimentally validating the mechanical property predictions of the framework, while challenging, will improve the reliability of the framework of use in the design and qualification for AM metals. Besides validation, it will also be important to incorporate residual stresses, surface roughness, and defects, such as pores, into the process model to yield more realistic predictive results. The

process model is currently limited to DLD, and the addition of simulating powder-bed processes would improve the flexibility of the framework. Furthermore, improvements can be made to the hardening model to account for slip transmissibility across grain boundaries. Future efforts will focus on addressing these shortcomings.

5. Conclusions

In this work, a semi-automated, multi-scale, multi-physics modeling framework is developed for prediction of the effective mechanical properties throughout metal AM build domains. The framework combines DLD process modeling with microstructure-sensitive mechanical modeling to generate effective mechanical property maps in regions of interest within the 3D build domain. First, the thermal history and resulting grain structure are simulated for a multi-pass, multi-layer DLD process. The simulated microstructures replicate physical AM microstructures found in the literature by varying different nucleation parameters used in the process model. Then, the micromechanical responses of numerous microstructural subvolumes within layers of interest are simulated using the parallelized EVPFFT code, MASSIF. Based on the homogenized stress–strain response of each subvolume, effective property maps are generated for the entire region of interest.

As a demonstration, the framework was applied to four different instantiations of DLD SS316L by manipulating the nucleation parameters. As the simulated grain structure transitioned from columnar (domain A) to equiaxed (domain D), visible patterns in the effective yield strength emerged in the resulting property maps, where the effective yield strength in the TD and BD directions for domain D was generally lower along the scan lines and higher in between scan lines. The same pattern was not apparent for loading in the SD direction of domain D, or for any loading scenarios of the columnar-grained microstructures. A slight anisotropy of the effective yield strength was observed, with the yield strength in the SD typically higher than the yield strength in the loading direction. This anisotropy and its variance decreased moving from domain A to domain D. Multiple hotspots were also visible throughout the results of the framework on the DLD SS316L microstructures. The framework clearly demonstrates that as the part is built pass by pass, if the microstructure is more uniform (as in domain D), the spatial variability in properties can be significantly reduced, and the effective yield strength generally becomes less anisotropic.

The process–(micro)structure–property framework provides a powerful tool that can be used to predict the location-specific variability in mechanical properties as well as the existence and location of potential hotspots in metal AM volumes, which could have a significant impact on the design and qualification process of metal AM structures. This framework helps to address a technical gap (namely Gap FMP5) that was identified in a recent roadmap for standardization of AM [57]. While currently limited to DLD and non-porous materials, an extension to simulate powder-bed processes and defects would allow design engineers to predict a multitude of realistic AM microstructures and the variability of their properties, which could aid in the endorsement of metal AM for critical structural applications.

Acknowledgments

ORCID iDs

Carl Herriott ⓘ https://orcid.org/0000-0001-5755-3245
Nadia Kouraytem ⓘ https://orcid.org/0000-0002-7183-2774
Benjamin Anglin ⓘ https://orcid.org/0000-0001-5501-116X
Anthony D Rollett ⓘ https://orcid.org/0000-0003-4445-2191
Ashley D Spear ⓘ https://orcid.org/0000-0002-3933-3131

References

[1] DebRoy T, Wei H, Zuback J, Mukherjee T, Elmer J, Milewski J, Beese A, Wilson-Heid A, De A and Zhang W 2018 Additive manufacturing of metallic components—process, structure and properties *Prog. Mater. Sci.* **92** 112–224

[2] Song B, Zhao X, Li S, Han C, Wei Q, Wen S, Liu J and Shi Y 2015 Differences in microstructure and properties between selective laser melting and traditional manufacturing for fabrication of metal parts: a review *Front. Mech. Eng.* **10** 111–25

[3] Beuth J *et al* 2013 Process mapping for qualification across multiple direct metal additive manufacturing processes *Proc. SFF Symp. (Austin, TX)* pp 12–4

[4] Montgomery C, Beuth J, Sheridan L and Klingbeil N 2015 Process mapping of Inconel 625 in laser powder bed additive manufacturing *Solid Freeform Fabrication Symp.* pp 1195–204

[5] Gockel J, Beuth J and Taminger K 2014 Integrated control of solidification microstructure and melt pool dimensions in electron beam wire feed additive manufacturing of Ti-6Al-4V *Additive Manuf.* **1** 119–26

[6] Clymer D R, Cagan J and Beuth J 2017 Power-velocity process design charts for powder bed additive manufacturing *J. Mech. Des.* **139** 100907

[7] Mohsen S, Daniel C, Jack B, Ola H and Lewandowski J J 2016 Process mapping, fracture and fatigue behavior of Ti-6Al-4V produced by EBM additive manufacturing *Proc. of the 13th World Conf. on Titanium* (Hoboken, NJ: Wiley-Blackwell) pp 1373–7

[8] Dehoff R, Kirka M, Sames W, Bilheux H, Tremsin A, Lowe L and Babu S 2015 Site specific control of crystallographic grain orientation through electron beam additive manufacturing *Mater. Sci. Technol.* **31** 931–8

[9] Jared B H, Aguilo M A, Beghini L L, Boyce B L, Clark B W, Cook A, Kaehr B J and Robbins J 2017 Additive manufacturing: toward holistic design *Scr. Mater.* **135** 141–7

[10] Kappes B, Moorthy S, Drake D, Geerlings H and Stebner A 2018 Machine learning to optimize additive manufacturing parameters for laser powder bed fusion of inconel 718 *Proc. 9th Int. Symp. on Superalloy 718 & Derivatives: Energy, Aerospace, and Industrial Applications* (Berlin: Springer) pp 595–610

[11] Yan W, Lian Y, Yu C, Kafka O L, Liu Z, Liu W K and Wagner G J 2018 An integrated process-structure-property modeling framework for additive manufacturing *Comput. Methods Appl. Mech. Eng.* **339** 184–204

[12] Zhang J, Liou F, Seufzer W and Taminger K 2016 A coupled finite element cellular automaton model to predict thermal history and grain morphology of Ti-6Al-4V during direct metal deposition (DMD) *Additive Manuf.* **11** 32–9

[13] Rai A, Helmer H and Körner C 2017 Simulation of grain structure evolution during powder bed based additive manufacturing *Additive Manuf.* **13** 124–34

[14] Lópeza O, Martinez-Hernandezb U, Ramírezc J, Pinnaa C and Mumtaza K 2016 Two-dimensional simulation of grain structure growth within selective laser melted AA-2024 *Mater. Des.* **113** 369–76

[15] Zinovieva O, Zinoviev A and Ploshikhin V 2018 Three-dimensional modeling of the microstructure evolution during metal additive manufacturing *Comput. Mater. Sci.* **141** 207–20

[16] Panwisawas C, Qiu C, Anderson M J, Sovani Y, Turner R P, Attallah M M, Brooks J W and Basoalto H C 2017 Mesoscale modelling of selective laser melting: thermal fluid dynamics and microstructural evolution *Comput. Mater. Sci.* **126** 479–90

[17] Rodgers T M, Madison J D and Tikare V 2017 Simulation of metal additive manufacturing microstructures using kinetic Monte Carlo *Comput. Mater. Sci.* **135** 78–89

[18] Li X and Tan W 2018 Numerical investigation of effects of nucleation mechanisms on grain structure in metal additive manufacturing *Comput. Mater. Sci.* **153** 159–69

[19] Hedayati R, Hosseini-Toudeshky H, Sadighi M, Mohammadi-Aghdam M and Zadpoor A 2016 Computational prediction of the fatigue behavior of additively manufactured porous metallic biomaterials *Int. J. Fatigue* **84** 67–79

[20] Taheri Andani M *et al* 2016 Achieving biocompatible stiffness in NiTi through additive manufacturing *J. Intell. Mater. Syst. Struct.* **27** 2661–71

[21] Leuders S, Vollmer M, Brenne F, Tröster T and Niendorf T 2015 Fatigue strength prediction for titanium alloy TiAl6V4 manufactured by selective laser melting *Metall. Mater. Trans.* A **46** 3816–23

[22] Zhang M, Sun C-N, Zhang X, Wei J, Hardacre D and Li H 2018 Predictive models for fatigue property of laser powder bed fusion stainless steel 316L *Mater. Des.* **145** 42–54

[23] Miranda G, Faria S, Bartolomeu F, Pinto E, Madeira S, Mateus A, Carreira P, Alves N, Silva F and Carvalho O 2016 Predictive models for physical and mechanical properties of 316L stainless steel produced by selective laser melting *Mater. Sci. Eng.* A **657** 43–56

[24] Collins P C, Haden C V, Ghamarian I, Hayes B J, Ales T, Penso G, Dixit V and Harlow G 2014 Progress toward an integration of process-structure-property-performance models for 'Three-Dimensional (3-D) Printing' of titanium alloys *JOM* **66** 1299–309

[25] Hayes B J *et al* 2017 Predicting tensile properties of Ti-6Al-4V produced via directed energy deposition *Acta Mater.* **133** 120–33

[26] Ozturk T and Rollett A D 2018 Effect of microstructure on the elasto-viscoplastic deformation of dual phase titanium structures *Comput. Mech.* **61** 55–70

[27] Ahmadi A, Mirzaeifar R, Moghaddam N S, Turabi A S, Karaca H E and Elahinia M 2016 Effect of manufacturing parameters on mechanical properties of 316L stainless steel parts fabricated by selective laser melting: a computational framework *Mater. Des.* **112** 328–38

[28] Andani M T, Karamooz-Ravari M R, Mirzaeifar R and Ni J 2018 Micromechanics modeling of metallic alloys 3D printed by selective laser melting *Mater. Des.* **137** 204–13

[29] Gandin C-A, Desbiolles J-L, Rappaz M and Thevoz P 1999 A three-dimensional cellular automation-finite element model for the prediction of solidification grain structures *Metall. Mater. Trans.* A **30** 3153–65

[30] King W, Anderson A, Ferencz R, Hodge N, Kamath C, Khairallah S and Rubenchik A 2015 Laser powder bed fusion additive manufacturing of metals; physics, computational, and materials challenges *Appl. Phys. Rev.* **2** 041304

[31] Wen S and Shin Y C 2010 Modeling of transport phenomena during the coaxial laser direct deposition process *J. Appl. Phys.* **108** 044908

[32] Tan W and Shin Y C 2015 Multi-scale modeling of solidification and microstructure development in laser keyhole welding process for austenitic stainless steel *Comput. Mater. Sci.* **98** 446–58

[33] Rappaz M and Gandin C-A 1993 Probabilistic modelling of microstructure formation in solidification processes *Acta Metall. Mater.* **41** 345–60

[34] Gäumann M, Bezencon C, Canalis P and Kurz W 2001 Single-crystal laser deposition of superalloys: processing-microstructure maps *Acta Mater.* **49** 1051–62

[35] Groeber M A, Jackson M A and DREAM 3D 2014 A digital representation environment for the analysis of microstructure in 3D *Integr. Mater. Manuf. Innov.* **3** 5

[36] Groeber M, Ghosh S, Uchic M D and Dimiduk D M 2008 A framework for automated analysis and simulation of 3D polycrystalline microstructures: I. Statistical characterization *Acta Mater.* **56** 1257–73

[37] Beaudoin A Jr, Mecking H and Kocks U 1996 Development of localized orientation gradients in fcc polycrystals *Phil. Mag.* A **73** 1503–17

[38] Mika D P and Dawson P R 1998 Effects of grain interaction on deformation in polycrystals *Mater. Sci. Eng.* A **257** 62–76

[39] Zhao Z, Ramesh M, Raabe D, Cuitino A and Radovitzky R 2008 Investigation of three-dimensional aspects of grain-scale plastic surface deformation of an aluminum oligocrystal *Int. J. Plast.* **24** 2278–97

[40] Lebensohn R A 2001 N-site modeling of a 3D viscoplastic polycrystal using fast Fourier transform *Acta Mater.* **49** 2723–37

[41] Michel J, Moulinec H and Suquet P 2000 A computational method based on augmented Lagrangians and fast Fourier transforms for composites with high contrast *Comput. Modelling Eng. Sci.* **1** 79–88

[42] Moulinec H and Suquet P 1998 A numerical method for computing the overall response of nonlinear composites with complex microstructure *Comput. Methods Appl. Mech. Eng.* **157** 69–94

[43] Mura T 2013 *Micromechanics of Defects in Solids* (Dordrecht: Springer Science & Business Media)

[44] Prakash A and Lebensohn R 2009 Simulation of micromechanical behavior of polycrystals: finite elements versus fast Fourier transforms *Modelling Simul. Mater. Sci. Eng.* **17** 064010

[45] Sintay S D 2010 Statistical microstructure generation and 3D microstructure geometry extraction *PhD Thesis* Carnegie Mellon University

[46] Lebensohn R A, Kanjarla A K and Eisenlohr P 2012 An elasto-viscoplastic formulation based on fast Fourier transforms for the prediction of micromechanical fields in polycrystalline materials *Int. J. Plast.* **32** 59–69

[47] Chakravarthy S S and Curtin W 2011 Stress-gradient plasticity *Proc. Natl Acad. Sci.* **108** 15716–20

[48] The HDF Group 1997–2018 Hierarchical Data Format, version 5 (http://hdfgroup.org/HDF5)

[49] Tari V, Lebensohn R A, Pokharel R, Turner T J, Shade P A, Bernier J V and Rollett A D 2018 Validation of micro-mechanical FFT-based simulations using high energy diffraction microscopy on Ti-7Al *Acta Mater.* **154** 273–83

[50] Ballard D H 1987 Generalizing the Hough transform to detect arbitrary shapes *Readings in Computer Vision* (Amsterdam: Elsevier) pp 714–25

[51] Ledbetter H M 1984 Monocrystal-polycrystal elastic constants of a stainless steel *Phys. Status Solidi* a **85** 89–96

[52] Upadhyay M V, Capek J, Van Petegem S, Lebensohn R A and Van Swygenhoven H 2017 Intergranular strain evolution during biaxial loading: a multiscale FE-FFT approach *JOM* **69** 839–47

[53] Ma M, Wang Z, Wang D and Zeng X 2013 Control of shape and performance for direct laser fabrication of precision large-scale metal parts with 316L stainless steel *Opt. Laser Technol.* **45** 209–16

[54] Zietala M *et al* 2016 The microstructure, mechanical properties and corrosion resistance of 316L stainless steel fabricated using laser engineered net shaping *Mater. Sci. Eng.* A **677** 1–10

[55] Li J, Deng D, Hou X, Wang X, Ma G, Wu D and Zhang G 2016 Microstructure and performance optimisation of stainless steel formed by laser additive manufacturing *Mater. Sci. Technol.* **32** 1223–30

[56] Moverare J J and Odén M 2002 Influence of elastic and plastic anisotropy on the flow behavior in a duplex stainless steel *Metall. Mater. Trans.* A **33** 57–71

[57] America Makes and ANSI Additive Manufacturing Standardization Collaborative (AMSC) 2018 Standardization Roadmap for Additive Manufacturing, version 2